Applications of X-Ray Computed Tomography in Particulate Systems †

C. L. Lin, J. D. Miller, and A. Cortes
*Comminution Center, University of Utah**

Abstract

X-ray computed tomography (CT) is an ideal technique for investigating the internal structure of multiphase materials in a noninvasive and nondestructive manner. CT technology used in conjunction with specialized algorithms and advanced computer facilities can be used to provide quantitative information in addition to being an ideal medium for scientific visualization. This paper reviews some advanced reconstruction algorithms and examines two cases in which CT has been successfully used : (1) coal washability analysis and (2) density gradient determination in an air-sparged hydrocyclone (ASH) flotation.

Introduction

X-ray computed tomography (CT) technique had its origin in the medical services[1-] and is now being applied to non-medical and industrial applications[2-]. CT techniques have an inherent advantage in providing very detailed images of the internal structures of opaque materials in a nondestructive manner. Nevertheless, most of the industrial applications of CT are qualitative in nature, probably a carry over from its use in the medical field. It should be noted that CT images contain enough information to allow for the quantitative description of the object being analyzed.

This paper is divided into two major sections, the first section covers the theoretical aspects of tomography and the numerical algorithms necessary for image reconstruction. The second section deals with some examples of quantitative X-ray CT applications in particulate processing.

Fundamental Principles

Basic Theory

The relationship between the initial intensity of an X-ray beam as it leaves the source and the final intensity of the same beam after it has passed through a section of the target material can be described by the following equation.

$$I_f = I_i \exp\left[-\int_{Ray} \mu(x,y)ds\right] \quad (1)$$

where :

I_i = initial intensity of the X-ray beam
I_f = final intensity of the X-ray beam
μ = linear attenuation coefficient.

Figure 1 illustrates the above mentioned equation.

An important assumption that was made implicitly in Equation 1 is that the X-ray beam

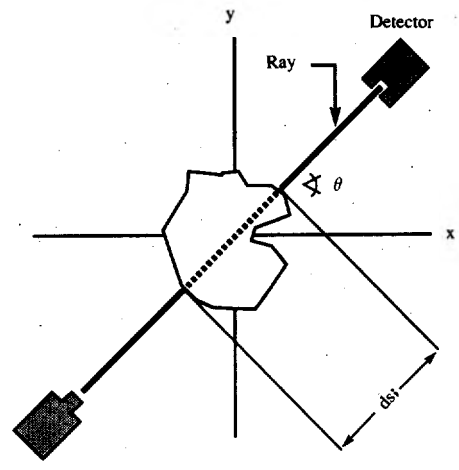

Fig. 1 A diagram showing an X-ray beam as it emanates from the source, passes through the sample, and finally is collected at the detector.

* 306, WBB Salt Lake City. Utah 84112, USA
† Received July 1992.

intensity is monochromatic in nature. This is not strictly true. Rearranging Equation 1 in the following manner,

$$ln\left[\frac{I_i}{I_f}\right]=\int_{Ray}\mu(x,y)ds \qquad (2)$$

shows that the left-hand side of Equation 2 is a measured quantity. This value can be obtained from the CT machine. The right-hand side of Equation 2 represents the ray integral of the X-ray beam that passed through the sample. If Ray is defined as follows:

$$x\cos\theta-y\sin\theta=Ray \qquad (3)$$

then the line integral can be written in the following manner.

$$P_\theta(Ray)=\int_{Ray}f(x,y)ds \qquad (4)$$

where:

$P_\theta(Ray)$ = is the projection of the X-ray beam that passes through the sample.

Notice that the right-hand side of Equation 4 is essentially the same as the right-hand side of Equation 2. The unknown function $f(x,y)$ simply takes the place of the linear attenuation coefficient $\mu(x,y)$. By using the definition of the Dirac delta function, Equation 4 can be reformulated as:

$$P_\theta(Ray)=\int_{-\infty}^{\infty}\int_{-\infty}^{\infty}f(x,y)\delta(x\cos\theta-y\sin\theta-Ray)dxdy \qquad (5)$$

Equation 5 is known as the Radon transform of the function $f(x,y)$. If we pass a series of line integrals through the unknown function $f(x,y)$ at a fixed angle θ, we obtain what is called a projection $P(\theta)$. This is shown in **Figure 2**.

$P(\theta)$ can be obtained by using an assemblage of sources and detectors and translating them at predefined intervals until they cover the entirety of the sample being scanned. In order to correlate the projection $P(\theta)$ to a reconstructed X-ray CT image, we need to use the properties of Fourier transforms[3]. Although a very simplified and conceptual approach will be presented here, a more rigorous mathematical treatment can be found in standard texts[4,5]. Furthermore, the treatment here will be confined to the case of parallel-beam geometry. Other geometries are treated in the references cited.

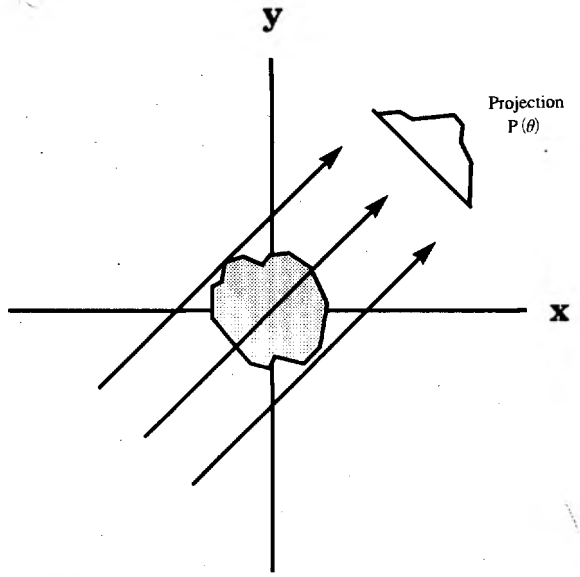

Fig. 2 An illustration showing several rays traversing through the sample at a fixed angle. The data from the series of rays are called a projection P(θ).

If a 2-D Fourier transform is performed on a function $f(x,y)$, Equation 6 would be the result.

$$F(u,v)=\int_{-\infty}^{\infty}\int_{-\infty}^{\infty}f(x,y)e^{-j2\pi(ux+vy)}dxdy \qquad (6)$$

This is illustrated in **Figure 3**. The shaded circle in **Figure 3** is the two-dimensional Fourier transform of the function $f(x,y)$. The transformed coordinates are designated as u and v.

Similarly, if a 1-D Fourier transform is performed on the projection data $P(\theta)$, Equation 7 would result.

$$S_\theta(\omega)=\int_{-\infty}^{\infty}P(\theta,t)e^{-j2\pi\omega t}dt \qquad (7)$$

To relate the 1-D Fourier transform of the projection of an unknown function $f(x,y)$ to the 2-D Fourier transform of the same unknown function, we make use of the Fourier Slice Theorem[5]. As an illustration, for the angle of measurement $\theta=0$, Equation 6 reduces to

$$F(u,v)|_{\theta=0}=\int_{-\infty}^{\infty}P(0,x)e^{-2\pi(ux)}dx \qquad (8)$$

The right-hand side of Equation 8 is just Equation 7 measured at $\theta=0$. To help in visualizing the relationship of Equation 7 to Equation 8, refer to **Figure 4**. **Figure 4** shows that if a 1-D Fourier transform is performed on projection $P(\theta)$, the result would correspond to the

data points in the line at an angle θ in the transformed coordinate axes u and v. The u and v coordinate system represents the 2-D Fourier transform of the unknown function $f(x, y)$. This is the same coordinate system shown in **Figure 3**.

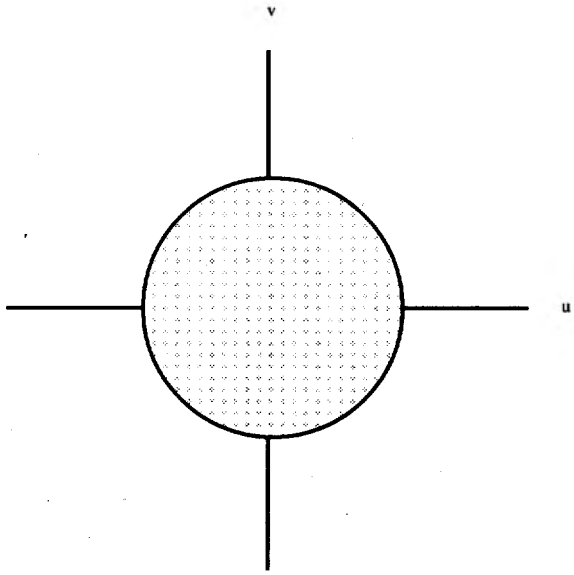

Fig. 3 An illustration showing the function f(x,y) after it undergoes a 2-D Fourier transform operation. The transformed coordinate system is designated by variables u and v.

By extension of logic, it can be concluded that, to construct a 2-D Fourier transform of an unknown function, one has to collect projection data at different angles, perform a 1-D Fourier transform on the projection data and finally plot the data on the u and v coordinate system. Once the 2-D Fourier map is completed, it is a simple matter of performing a 2-D inverse Fourier transform to reconstruct the image.

The above discussion provides a mathematical basis for the relationship between the projected data and the image reconstruction which is the foundation of CT technology. In practice, however, the above procedure is not followed. The reasons for deviating from the theoretical approach are twofold : 1) algorithm stability and 2) computational efficiency. **Figure 5** shows a block diagram for one of the procedures used to obtain an image from CT projection data. The first step is to collect the projection data from the CT machine. The next step is to perform a convolution between the projection data and a suitable filter. The filtered projection is then back-projected to obtain the reconstructed image. Additional image-processing techniques such as thresholding can be applied to obtain more pleasing images.

Back-projection is a discrete operation that mimics the operation of the CT machine but is done in the reverse manner. **Figure 6** shows a simplified illustration of the projection and back-projection operations. The upper part of **Figure 6** shows a sample conveniently subdivided into nine parts. The apparent density of each part is shown. If a ray is passed through the sample at an angle of 0 degrees, as shown by the broad gray-shaded line, it will report that the apparent density of the cross section that

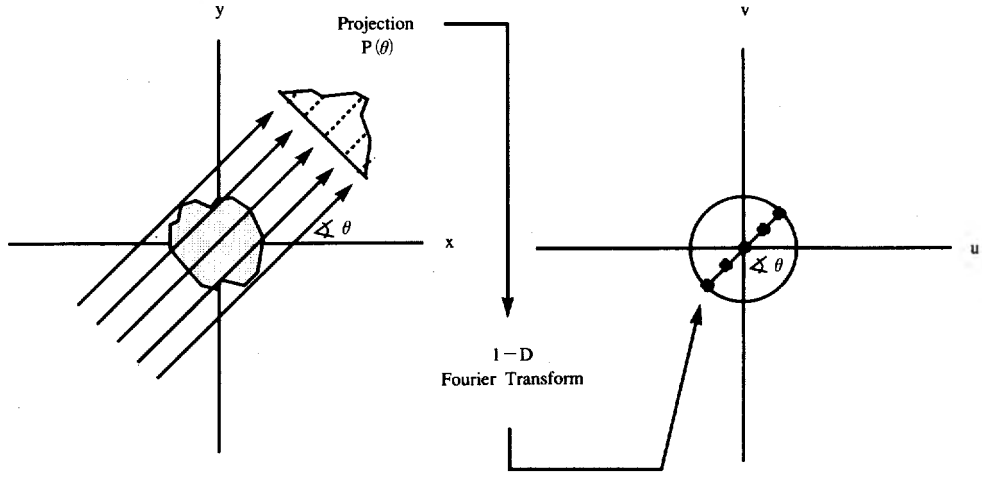

Fig. 4 A drawing showing how the 1-D Fourier transform of the projection P(θ) can be mapped into the 2-D domain of the transformed coordinate system.

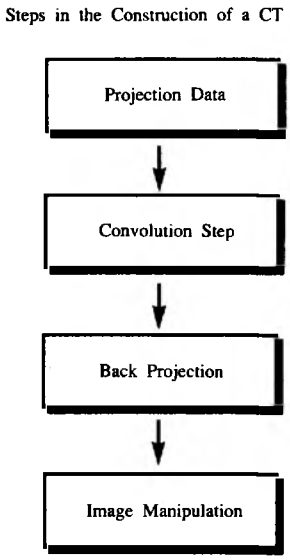

Fig. 5 A block diagram showing the steps necessary in the construction of an image obtained from a CT scanner.

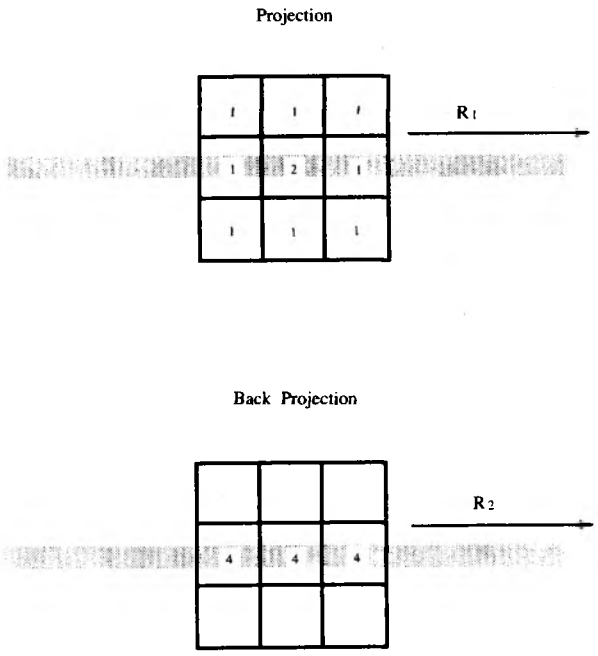

Fig. 6 An illustration showing how the projection operation determines the apparent density of the material that an X-ray beam traverses. The lower drawing shows how the back-projection operation places the calculated density in the synthetic grid designed to represent the sample being scanned.

has been traversed is 4. The value 4 represents the projected density through the middle of the sample at an angle 0 given by ray R_1. During the back-projection operation, R_2 traverses a grid designed to represent the sample being scanned and places the value 4 on all the blocks it intersects. The geometric characteristics of R_2 (location and angle) are precisely the same as R_1. At first glance, it appears that the results of the reproduction operation are very different from the values of the original sample. However, if the projection and back-projection operations are performed using a large number of angles and if the final back-projected image is normalized by the number of angles used, the reconstructed image approximates the original sample.

Advanced Reconstruction Algorithm

In order to obtain more accurate reconstruction of tomographic images, a new algorithm is being developed[6]. This algorithm draws from the strength of the filtered back-projection methods but is iterative in nature. This approach allows for the inclusion of *a priori* information into the solution. A block diagram of the unit operations involved in the algorithm is shown in **Figure 7**. The basic steps in the new algorithm are as follows :

1. Obtain the projection data (sinograms) from the CT machine.
2. Convolve the projections with a suitable filter.
3. Perform the back-projection.
4. Normalize the resulting image.
5. Use a synthetic projector to create a new set of projection data from the reconstructed image.
6. Compare the new set of projection data with the original data from step 1.
7. Generate a set of error vectors.
8. Back-project the generated error vectors to form an error image.
9. Combine the error image with the original image to create a corrected image. If satisfied terminate the iteration, otherwise go back to step 5.

The unit operations enclosed in the dashed-lined block represent the steps normally present in a conventional CT reconstruction. All other unit operations shown represent enhancements that are introduced by the new algorithm.

The effectiveness of the new algorithm was

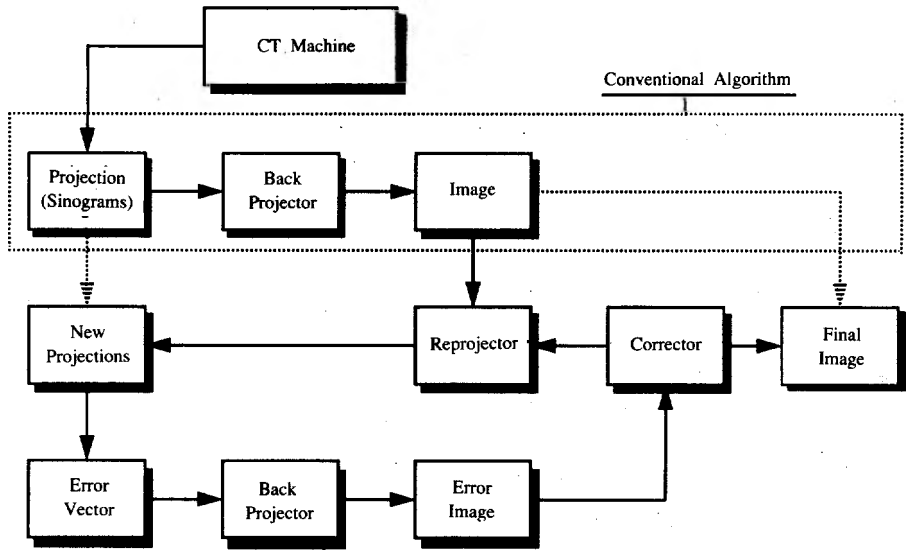

Fig. 7 A block diagram showing the various operations of the advanced algorithm. The operations enclosed in the dotted rectangle represent operations that are present in the conventional CT reconstruction algorithm.

tested by performing a numerical simulation. The simulation pattern consisted of three concentric squares. This test pattern is shown in **Figure** 8. The outermost square has a density of 4.0 g/cc, the middle square has a density of 2.0 g/cc and the innermost square has a density of 8.0 g/cc. The test pattern was chosen so that streaks emanating from the high-density square could be easily seen. The simulation was done using a 256 × 256 computational grid. All calculations were performed using a Stardent 3040 graphics workstation.

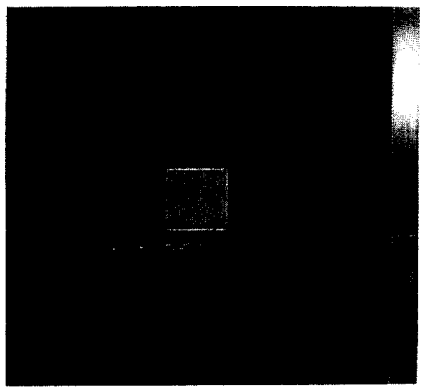

Fig. 8 The image used to test the applicability of the advanced reconstruction algorithm.

In order to quantify the overall reconstruction quality, a criterion called image error was defined. This represents the "distance" of the reconstructed image from the known original test pattern. The definition is given below.

$$Image\ Error = \sqrt{\frac{(original\ image - reconstructed\ image)^2}{original\ image^2}} \qquad (9)$$

where,

original image = the density values of the test pattern

reconstructed image = the density values of the reconstructed image.

Table 1 presents the image errors calculated from a conventional filtered back-projection algorithm and from the new algorithm. The number of iterations used was 3. The results show that the new algorithm was able to reduce the reconstruction error by a factor of 2.

Table 1 Comparison of image errors obtained from the conventional filtered back-projection method and from the new algorithm after 3 iterations

	Conventional	New Algorithm
Image Error	0.0791	0.0328

Particulate Processing Applications

Coal Washability

Coal quality is determined, to a large extent,

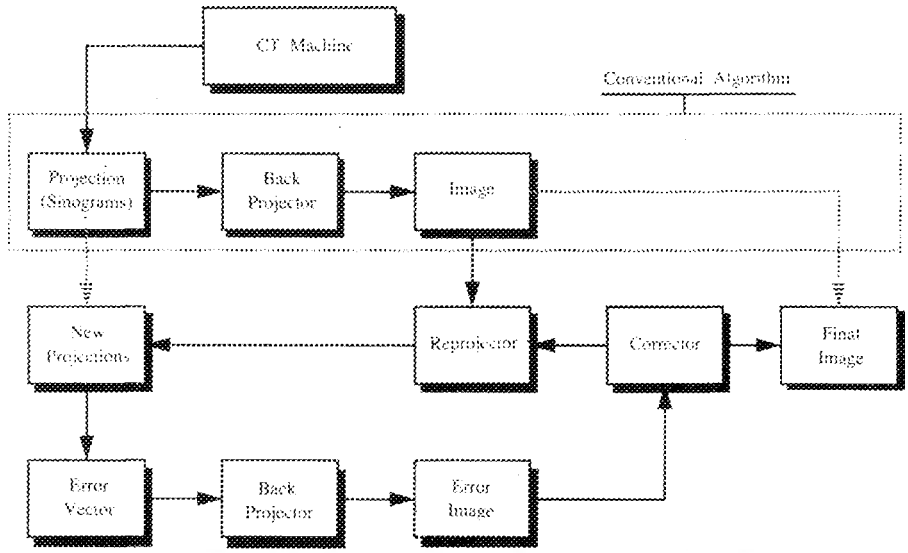

Fig. 7 A block diagram showing the various operations of the advanced algorithm. The operations enclosed in the dotted rectangle represent operations that are present in the conventional CT reconstruction algorithm.

tested by performing a numerical simulation. The simulation pattern consisted of three concentric squares. This test pattern is shown in **Figure 8**. The outermost square has a density of 4.0 g/cc, the middle square has a density of 2.0 g/cc and the innermost square has a density of 8.0 g/cc. The test pattern was chosen so that streaks emanating from the high density square could be easily seen. The simulation was done using a 256 × 256 computational grid. All calculations were performed using a Stardent 3040 graphics workstation.

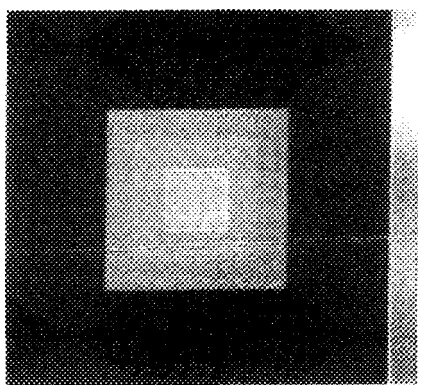

Fig. 8 The image used to test the applicability of the advanced reconstruction algorithm.

In order to quantify the overall reconstruction quality, a criterion called image error was defined. This represents the "distance" of the reconstructed image from the known original test pattern. The definition is given below.

$$Image\ Error = \sqrt{\frac{\sum (original\ image - reconstructed\ image)^2}{original\ image^2}} \qquad (9)$$

where,

original image = the density values of the test pattern

reconstructed image = the density values of the reconstructed image.

Table 1 presents the image errors calculated from a conventional filtered back-projection algorithm and from the new algorithm. The number of iterations used was 3. The results show that the new algorithm was able to reduce the reconstruction error by a factor of 2.

Table 1 Comparison of image errors obtained from the conventional filtered back-projection method and from the new algorithm after 3 iterations

	Conventional	New Algorithm
Image Error	0.0791	0.0328

Particulate Processing Applications

Coal Washability

Coal quality is determined, to a large extent,

by both its calorific value and its associated mineral-matter content. The mineral-matter impurities not only decrease the heating value of steam coal but are also responsible for maintenance and pollution problems during subsequent combustion. The mineral-matter dispersion gives rise to a continual variation in particle density best described by the washability curve. A coal-washability curve is important to the process engineer because it shows the limits of any physical separation of mineral matter from coal. Thus, the washability curve provides information on the expected quality of the clean coal product.

The conventional method for determining the washability curve is based on the series of sink-float separations using heavy liquids[7]. The steps that are necessary for this operation are as follows :

1. The coal sample is first sized into different size intervals, from 38 mm down to 0.1 mm.
2. For each size class, a suitable amount of sample is taken.
3. Then, dense liquid separations are performed for each size class-a series of binary fractionation based on density.
4. From the weight and analysis of each density fraction in step 3, the coal-washability curve for each size class is created.

In the case of X-ray CT-based washability calculation[8], the third step of the conventional approach is replaced by a series of steps based on CT scanning of the sample and 3-D reconstruction. Thus, in similar fashion, the steps needed in constructing a washability curve are as follows :

1. The coal sample is first sized into different size intervals, from 38 mm down to 0.1 mm.
2. For each size class, a suitable amount of sample is taken.
3. Density fractionation by CT analysis.
   a. Each sample is loaded into a separated cylindrical container, placed in the CT scanner and properly aligned.
   b. CT measurements (sequential scans) are taken as the container passes through the scanner in predetermined scan spacings.
   c. Computer analysis is performed on the scan data to determine the 2-D density data.
   d. The 2-D CT images (density data) are then used to reconstruct the particles in 3-D.
   e. The particles are isolated and the mass and volume of each particle is calculated.
4. From the weight and density calculations in step 3, the coal-washability curve for each size class is created.

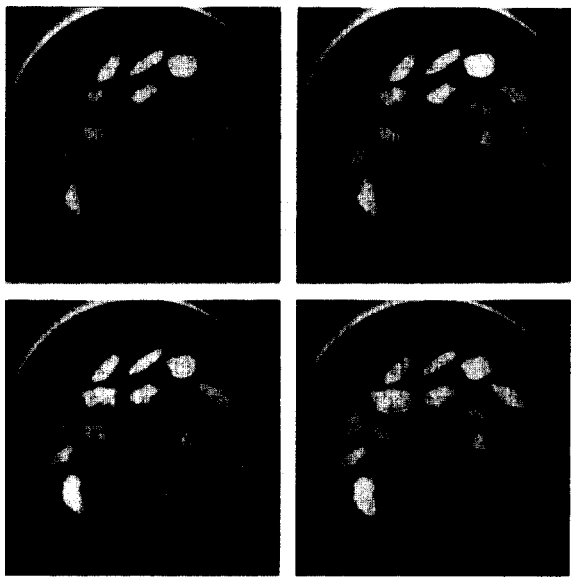

Fig. 9 Sequential 2-D X-ray CT scans of a coal sample. The grey-shaded bar at the right-hand side of the photograph represents the density scale in terms of CT number.

Figure 9 shows the sequential 2-D X-ray CT scan of the coal sample. The scale bar (CT number) located at the right-hand side of the figure indicates the relative density of the material. **Figure 10** shows the washability curve for the coal sample as obtained by both the conventional sink-float analysis and CT-based method. From these results, it is evident that coal-washability curves derived from the CT-based technique are in good agreement with the results obtained by the conventional sink-float analysis.

Air-Sparged Hydrocyclone (ASH) Flotation

The air-sparged hydrocyclone (ASH) is distinguished by its high-specific capacity for fine particle flotation in a centrifugal field. To elaborate, it is now evident that the ASH has a specific capacity of at least 100 times that of

by both its calorific value and its associated mineral-matter content. The mineral-matter impurities not only decrease the heating value of steam coal but are also responsible for maintenance and pollution problems during subsequent combustion. The mineral-matter dispersion gives rise to a continual variation in particle density best described by the washability curve. A coal-washability curve is important to the process engineer because it shows the limits of any physical separation of mineral matter from coal. Thus, the washability curve provides information on the expected quality of the clean coal product.

The conventional method for determining the washability curve is based on the series of sink-float separations using heavy liquids[7]. The steps that are necessary for this operation are as follows:

1. The coal sample is first sized into different size intervals, from 38 mm down to 0.1 mm.
2. For each size class, a suitable amount of sample is taken.
3. Then, dense liquid separations are performed for each size class-a series of binary fractionation based on density.
4. From the weight and analysis of each density fraction in step 3, the coal-washability curve for each size class is created.

In the case of X-ray CT based washability calculation[8], the third step of the conventional approach is replaced by a series of steps based on CT scanning of the sample and 3-D reconstruction. Thus, in similar fashion, the steps needed in constructing a washability curve are as follows:

1. The coal sample is first sized into different size intervals, from 38 mm down to 0.1 mm.
2. For each size class, a suitable amount of sample is taken.
3. Density fractionation by CT analysis.
   a. Each sample is loaded into a separated cylindrical container, placed in the CT scanner and properly aligned.
   b. CT measurements (sequential scans) are taken as the container passes through the scanner in predetermined scan spacings.
   c. Computer analysis is performed on the scan data to determine the 2-D density data.
   d. The 2-D CT images (density data) are then used to reconstruct the particles in 3-D.
   e. The particles are isolated and the mass and volume of each particle is calculated.
4. From the weight and density calculations in step 3, the coal-washability curve for each size class is created.

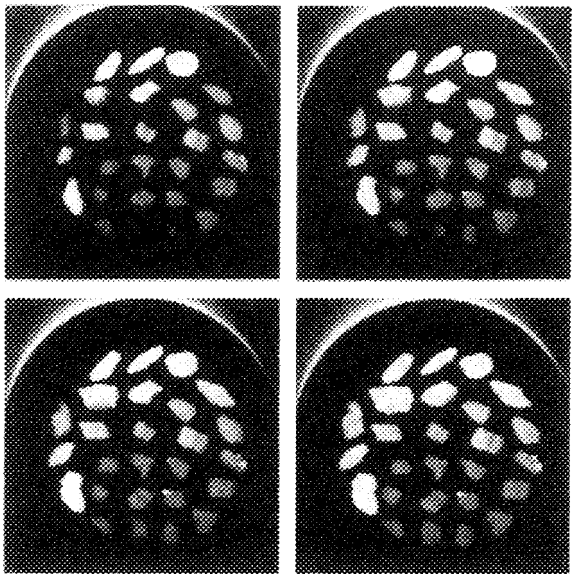

Fig. 9 Sequential 2-D X-ray CT scans of a coal sample. The grey-shaded bar at the right-hand side of the photograph represents the density scale in terms of CT number.

Figure 9 shows the sequential 2-D X-ray CT scan of the coal sample. The scale bar (CT number) located at the right-hand side of the figure indicates the relative density of the material. **Figure 10** shows the washability curve for the coal sample as obtained by both the conventional sink-float analysis and CT-based method. From these results, it is evident that coal-washability curves derived from the CT-based technique are in good agreement with the results obtained by the conventional sink-float analysis.

Air-Sparged Hydrocyclone (ASH) Flotation

The air-sparged hydrocyclone (ASH) is distinguished by its high-specific capacity for fine particle flotation in a centrifugal field. To elaborate, it is now evident that the ASH has a specific capacity of at least 100 times that of

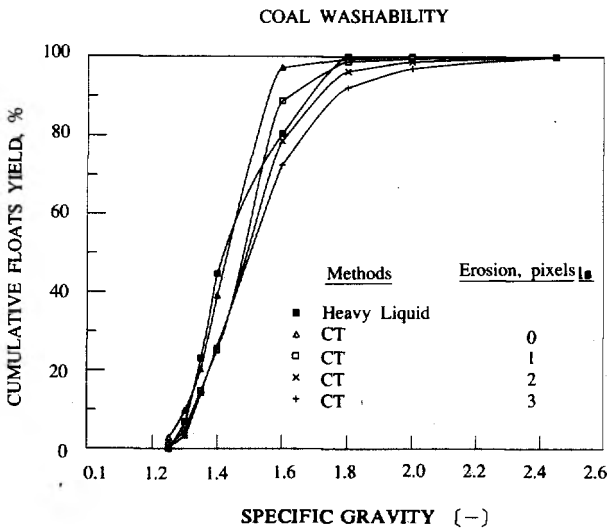

Fig. 10 A comparison of the coal-washability curve constructed using CT techniques with the coal-washability curve obtained by the traditional sink-float method.

conventional flotation equipment. The air-sparged hydrocyclone has shown promising potential for the flotation of copper porphyry ore, low-grade placer gold, auriferous pyrite ores, and various industrial minerals. Another promising application has been found to be the use of ASH for fine coal flotation. This has been demonstrated for a number of U.S. and Canadian coals. Also, attention has been given to applications of air-sparged hydrocyclone flotation technology outside of the mineral industry, including the pulp and paper industry and the food industry. The most significant development, however, is the construction of a 20-million dollar waste-paper recycling plant which will use ASH technology for the de-inking flotation.

A schematic diagram of the air-sparged hydrocylone is shown in **Figure 11**. The main features of the air-sparged hydrocyclone (ASH) are a porous tube through which air is sparged and a tangential flow of the particle suspension orthogonal to the airflow. The suspension passes downward through the separator in swirl flow and a counter-current flow of the froth phase moves upward and towards the center of the device. Hydrophilic particles are thrown against the porous tube wall by the centrifugal field and are discharged at the bottom as tailings. Hydrophobic particles encounter the air bubbles which are sparged radially through the porous wall. Particle/bubble attachment occurs, and the hydrophobic parti-

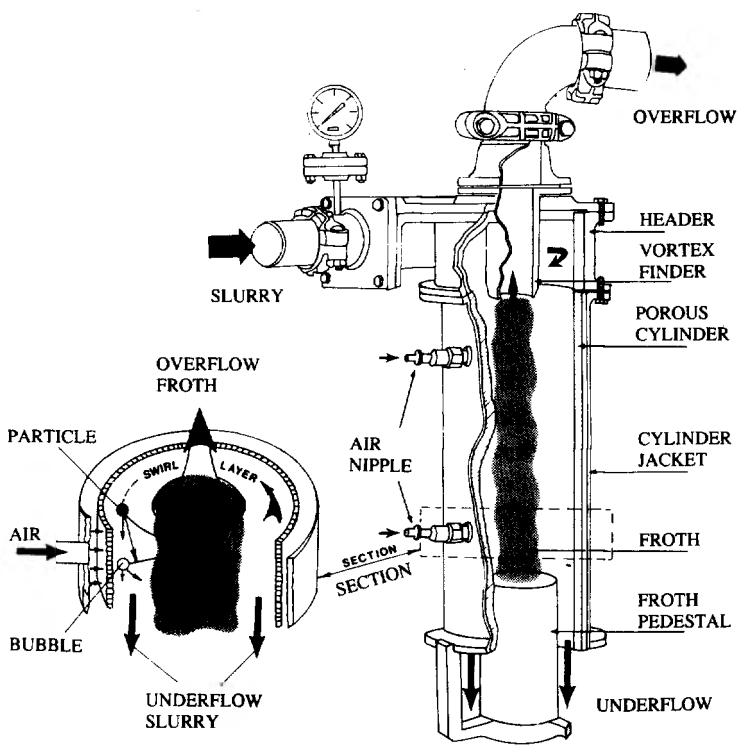

Fig. 11 A perspective drawing of the air-sparged hydrocyclone (ASH).

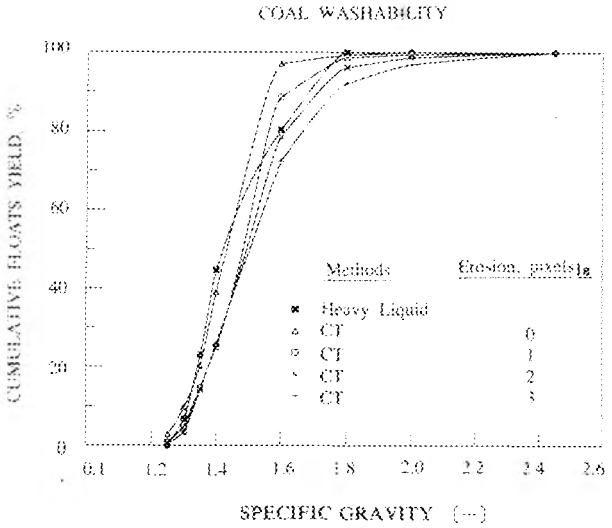

Fig. 10 A comparison of the coal-washability curve constructed using CT techniques with the coal-washability curve obtained by the traditional sink-float method.

conventional flotation equipment. The air-sparged hydrocyclone has shown promising potential for the flotation of copper porphyry ore, low-grade placer gold, auriferous pyrite ores, and various industrial minerals. Another promising application has been found to be the use of ASH for fine coal flotation. This has been demonstrated for a number of U.S. and Canadian coals. Also, attention has been given to applications of air-sparged hydrocyclone flotation technology outside of the mineral industry, including the pulp and paper industry and the food industry. The most significant development, however, is the construction of a 20-million dollar waste-paper recycling plant which will use ASH technology for the de-inking flotation.

A schematic diagram of the air-sparged hydrocylone is shown in **Figure 11**. The main features of the air-sparged hydrocylone (ASH) are a porous tube through which air is sparged and a tangential flow of the particle suspension orthogonal to the airflow. The suspension passes downward through the separator in swirl flow and a counter-current flow of the froth phase moves upward and towards the center of the device. Hydrophilic particles are thrown against the porous tube wall by the centrifugal field and are discharged at the bottom as tailings. Hydrophobic particles encounter the air bubbles which are sparged radially through the porous wall. Particle/bubble attachment occurs, and the hydrophobic parti-

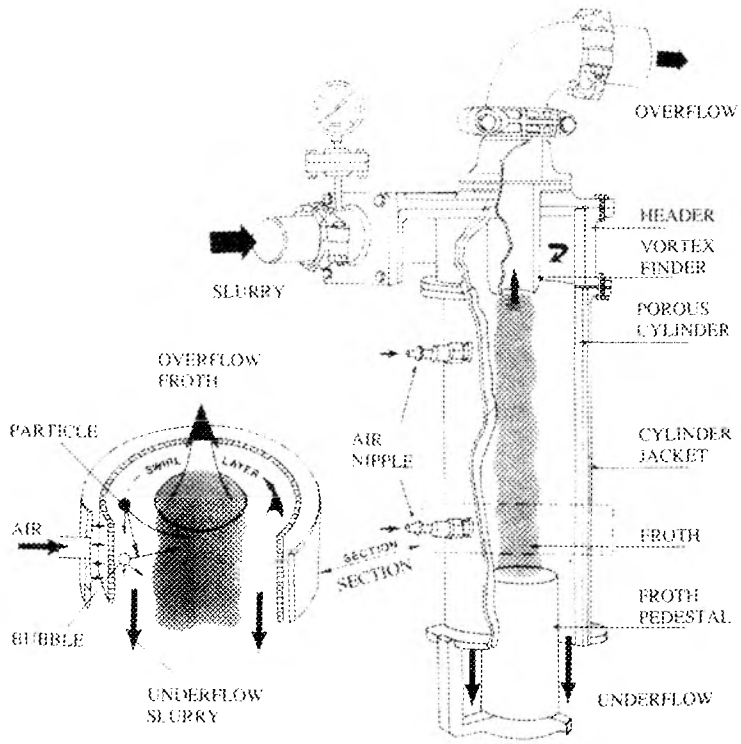

Fig. 11 A perspective drawing of the air-sparged hydrocyclone (ASH).

cles are transported into the froth phase which exits axially at the top of the cyclone through a vortex finder[9,10,11].

In order to gain a better understanding of how different particles are distributed inside the air-sparged hydrocyclone, CT scans have been performed on an operating ASH unit. **Figure 12** shows an example of the CT data obtained for a suspension of hydrophilic limestone particles (20% solids) flowing at 20 gpm with the air-flow rate of 200 slpm. In **Figure 12** the time-averaged density is plotted versus the position along a straight line for a particular cross-sectional scan of the ASH. By analyzing the scan sections made at different sections of the ASH, information regarding the density profile (time averaged) can be obtained. This information is being used to understand the fundamentals of the complex multiphase flow, optimize the operating conditions and thus improve the separation efficiency.

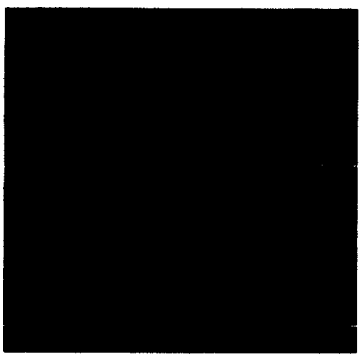

Fig. 12 ASH CT images with the reconstructed density of the segregated multiphase flow plotted with respect to radial position in the ASH at a particular elevation.

Conclusion

This paper demonstrates the effective use of CT technology in engineering applications, more specifically, to particulate systems. By using suitable algorithms, an alternative method of constructing the coal-washability curve has been developed. Furthermore, the time-averaged density profiles obtained from CT scans of an operating air-sparged hydrocyclone (ASH) have proved to be invaluable in helping to optimize the operating variables. Although the early results have been quite successful, much work needs to be done in the following areas : 1) advanced CT algorithms, 2) 3-D computer graphics, and 3) particle isolation algorithms.

Acknowledgement

The research has been supported by the Department of Interior's Mineral Institute program administered by the Bureau of Mines through the Generic Mineral Technology Center for Comminution under Grant No. G1105149. In addition, financial support from NSF Grant No. CTS 9000406 and DOE Grant No. DE FG22 90PCP0311 is gratefully acknowledged.

References

1) Herman, G. T. : Image Reconstruction from Projections : the Fundamentals of Computerized Tomography, Academic Press, New York (1980).
2) Banholzer, W. F. et al. : *Ind. Eng. Chem. Res.*, **Vol. 26**, pp. 763-767 (1987).
3) Boas, M. L. : Mathematical Methods in the Physical Sciences, John Wiley and Sons, New York (1983).
4) Rosenfeld, A. and Kak, A. C. : Digital Picture Processing, Second Edition, Academic Press, **Vol. 1** (1982).
5) Kak, A. C. and Slaney, M. : Principles of Computerized Tomographic Imaging, IEEE Press, New York (1988).
6) Cortes, A. B., Lin, C. L. and Miller, J. D. : Review of Progress in Nondestructive Evaluation, D. O. Thompson and D. E. Chimenti, Eds. **Vol. 10A**, Plenum Press, New York (1991).
7) Weiss, N. L. (Ed.) : SME Mineral Processing Handbook, AIME/SME, New York (1985).
8) Lin, C. L. et al. : *Coal Preparation*, **Vol. 9**, pp. 107-119 (1991).
9) Miller, J. D. et al. : XVI International Mineral Processing Congress, Stockholm, Sweden, E. Forssberg, Ed., Elsevier, Part A (1988).
10) Ye, Y. et al. : Proceedings International Column Flotation Symposium, AIME/SME, Phoenix, Chapter 34, pp. 305-313 (1988).
11) Miller, J. D. and Ye, Y. : Mineral Processing and Extractive Metallurgy Review, J. Laskowski, Ed., **Vol. 5**, pp. 307-329, Gordon and Breach, New York (1989).

cles are transported into the froth phase which exits axially at the top of the cyclone through a vortex finder[8,9,10,11].

In order to gain a better understanding of how different particles are distributed inside the air-sparged hydrocyclone, CT scans have been performed on an operating ASH unit. **Figure 12** shows an example of the CT data obtained for a suspension of hydrophilic limestone particles (20% solids) flowing at 20 gpm with the air-flow rate of 200 slpm. In **Figure 12** the time-averaged density is plotted versus the position along a straight line for a particular cross-sectional scan of the ASH. By analyzing the scan sections made at different sections of the ASH, information regarding the density profile (time averaged) can be obtained. This information is being used to understand the fundamentals of the complex multiphase flow, optimize the operating conditions and thus improve the separation efficiency.

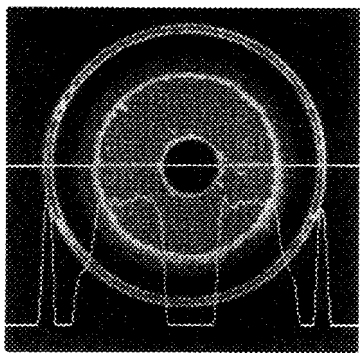

Fig. 12 ASH CT images with the reconstructed density of the segregated multiphase flow plotted with respect to radial position in the ASH at a particular elevation.

Conclusion

This paper demonstrates the effective use of CT technology in engineering applications, more specifically, to particulate systems. By using suitable algorithms, an alternative method of constructing the coal-washability curve has been developed. Furthermore, the time-averaged density profiles obtained from CT scans of an operating air-sparged hydrocyclone (ASH) have proved to be invaluable in helping to optimize the operating variables. Although the early results have been quite successful, much work needs to be done in the following areas: 1) advanced CT algorithms, 2) 3-D computer graphics, and 3) particle isolation algorithms.

Acknowledgement

The research has been supported by the Department of Interior's Mineral Institute program administered by the Bureau of Mines through the Generic Mineral Technology Center for Comminution under Grant No. G1105149. In addition, financial support from NSF Grant No. CTS 9000406 and DOE Grant No. DE FG22 90PCP0311 is gratefully acknowledged.

References

1) Herman, G. T.: Image Reconstruction from Projections: the Fundamentals of Computerized Tomography, Academic Press, New York (1980).
2) Banholzer, W. F. et al.: *Ind. Eng. Chem. Res.*, **Vol. 26**, pp. 763-767 (1987).
3) Boas, M. L.: Mathematical Methods in the Physical Sciences, John Wiley and Sons, New York (1983).
4) Rosenfeld, A. and Kak, A. C.: Digital Picture Processing, Second Edition, Academic Press, **Vol. 1** (1982).
5) Kak, A. C. and Slaney, M.: Principles of Computerized Tomographic Imaging, IEEE Press, New York (1988).
6) Cortes, A. B., Lin, C. L. and Miller, J. D.: Review of Progress in Nondestructive Evaluation, D. O. Thompson and D. E. Chimenti, Eds. **Vol. 10A**, Plenum Press, New York (1991).
7) Weiss, N. L. (Ed.): SME Mineral Processing Handbook, AIME/SME, New York (1985).
8) Lin, C. L. et al.: *Coal Preparation*, **Vol. 9**, pp. 107-119 (1991).
9) Miller, J. D. et al.: XVI International Mineral Processing Congress, Stockholm, Sweden, E. Forssberg, Ed., Elsevier, Part A (1988).
10) Ye, Y. et al.: Proceedings International Column Flotation Symposium, AIME/SME, Phoenix, Chapter 34, pp. 305-313 (1988).
11) Miller, J. D. and Ye, Y.: Mineral Processing and Extractive Metallurgy Review, J. Laskowski, Ed., **Vol. 5**, pp. 307-329, Gordon and Breach, New York (1989).